Progress In Electromagnetics Research, PIER 25, 131–165, 2000

SCATTERING FROM AXISYMMETRIC SCATTERERS: A HYBRID METHOD OF SOLVING MAUE'S EQUATION

J. G. Fikioris and A. N. Magoulas

Electrical & Computer Eng. Dept.
National Technical University of Athens
9 Iroon Polytechniou Str.
Zografou 15773, Greece

1. INTRODUCTION

The scattering of electromagnetic (EM) waves from perfectly conducting or dielectric scatterers of arbitrary shape can be formulated in terms of singular surface integral equations for the tangential components of the total electric $\vec{E}$ and magnetic $\vec{H}$ fields on the scatterer surface S. The integrals involved can be shown to be convergent for smooth enough S (for instance, when the normal on S is continuous) [1–4]. In this paper the study is restricted to perfectly conducting scatterers without edges; as unknown serves the surface current density $\vec{J}(\vec{r})$ induced on S, in other words the tangential component of the total $\vec{H}$ field. Two equivalent forms of the surface integral equation, known as Maue's equation, can be obtained [2, 4–6]; one of them involves, beyond $\vec{J}(\vec{r})$, its surface divergence $\nabla_S \cdot \vec{J}(\vec{r})$ and is less

convenient for numerical computations. The more common form reads as follows [1–6]:

$$\frac{1}{2}\vec{J}(\vec{r}) - \frac{1}{4\pi}\iint\limits_S \hat{n}(\vec{r}) \times \left[\vec{J}(\vec{r}\,') \times \nabla' G(R)\right] dS' = \hat{n}(\vec{r}) \times \vec{H}^{\text{inc}}(\vec{r}) \quad (1)$$

in which $\vec{r}$ is a fixed point on S, $\vec{r}\,'$ a variable point of integration on S, $\vec{H}^{\text{inc}}$ the incident EM wave, $R = |\vec{r} - \vec{r}\,'|$, $G(R) = \exp(jkR/R)$, $k = 2\pi/\lambda$ the wavenumber and $\hat{n}(\vec{r})$ the outward unit normal on S at $\vec{r}$. The time dependence is assumed to be $\exp(-j\omega t)$. The surface integral in (1) is improper, but, under certain conditions on $\vec{J}(\vec{r})$, it can be shown to be convergent [4, 7], the singularity of its integrand not exceeding that of $1/R'$, R' being the length of the projection of $|\vec{r}\,' - \vec{r}|$ on the plane tangent to S at $\vec{r}$ [7]. These facts are born out by the explicit results obtained later for the "self-patch" contribution to the integral in (1) and provide a first and necessary test of the correctness of the analytic evaluation of this all important contribution.

From this point on the analysis is further restricted to surfaces S of revolution around an axis z, as shown in Figure 1. In this case S is completely defined by the given functions $\rho = \rho(\ell)$, $z = z(\ell)$, where ℓ measures arc length along the generating curve of S from $\ell = 0$ to $\ell = L$.

This description of circularly symmetric S's by single-variable functions simplifies their representation and provides a good starting and quite general case for the analytic evaluation of certain surface integrals. The smoothness restrictions on S imply continuous $\rho'(\ell)$, $z'(\ell)$ and bounded $\rho''(\ell)$, $z''(\ell)$. In this case Maue's equation (1) splits into two integral equations for the azimuthal J_φ and meridian J_t components of $\vec{J}$:

$$\frac{1}{2}J_\varphi(\vec{r}) + H_t^{\text{inc}}(\vec{r}) = \frac{1}{4\pi}\iint\limits_S dS' \left\{ -\frac{\partial G}{\partial n}\left[\hat{\varphi}(\vec{r}) \cdot \vec{J}(\vec{r}\,')\right] + \frac{1}{\rho}\frac{\partial G}{\partial \varphi}\left[\hat{n}(\vec{r}) \cdot \vec{J}(\vec{r}\,')\right]\right\} \quad (2)$$

$$\frac{1}{2}J_t(\vec{r}) - H_\varphi^{\text{inc}}(\vec{r}) = \frac{1}{4\pi}\iint\limits_S dS' \left\{ -\frac{\partial G}{\partial n}\left[\hat{t}(\vec{r}) \cdot \vec{J}(\vec{r}\,')\right] + \frac{\partial G}{\partial t}\left[\hat{n}(\vec{r}) \cdot \vec{J}(\vec{r}\,')\right]\right\} \quad (3)$$

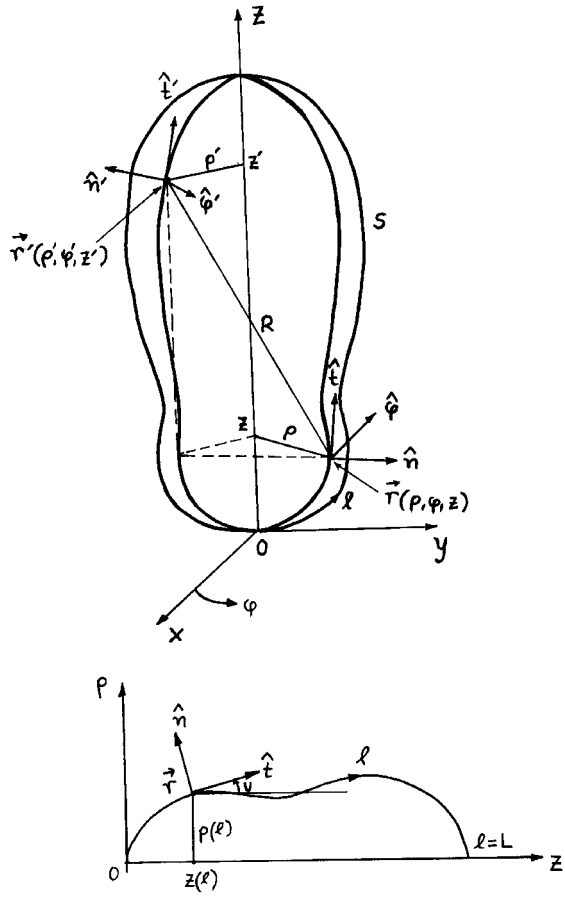

Figure 1. The axisymmetric scatterer configuration and its generating curve.

Dividing the intervals $0 \leq \varphi \leq 2\pi$ and $0 \leq \ell \leq L$ into N_φ and N_ℓ smaller ones, not necessarily equal, we divide S into about $N = N_\varphi N_\ell$ "trapezoidal" surface elements, or patches, $\Delta S = \rho \Delta \ell \Delta \varphi$. Around the top and bottom points $\ell = L, 0$ small cyclical patches are used. For numerical computations difficulties arise when $\vec{r}$ and $\vec{r}'$ belong to the same patch, or to adjacent ones, i.e., when R is comparable to the largest cord d' of $\Delta S'$ and, in particular for the self-patch, becomes even zero in the course of integration. This has been recognized by a number of authors; owing to similarities with our approach we cite in this connection two papers by E. Marx [8, 9]. We face these

difficulties by a hybrid (analytical-numerical) method: When $R \gg d'$, i.e., when $\vec{r}$ and $\vec{r}'$ are far apart, we replace R by the constant distance $R_c = |\vec{r} - \vec{r}'_c|$ ($\vec{r}'_c$ being the center of the patch over which we integrate) and reduce the surface integrals in (2), (3) to trivial ones. It is understood that $d' \ll \lambda$ and that $\vec{J}(\vec{r}')$ is practically constant over $\Delta S'$, equal to $\vec{J}(\vec{r}'_c)$. We call this mode of evaluating the surface integrals in (2), (3) "mode **A**". When R is comparable to d', $\vec{r}$ and $\vec{r}'$ belong to the same or to adjacent patches and the contribution to the surface integrals of (2), (3) from the self-patch and its adjacent ones are evaluated analytically using local Taylor expansions of the numerators and denominators of the integrands in (2), (3) around the point of evaluation $\vec{r}(\ell, \varphi)$ and retaining only their leading terms. We call this mode of evaluating the surface integrals "mode **B**". It is remarkable that the self-patch integrals, although improper, turn out to be explicitly convergent, i.e., they vanish with $\Delta S'$ no matter how the latter shrinks to zero. This is required by theory [7], since self-patch integrals cannot be evaluated by principal-value approaches, $1/R$, $1/R^3$ etc. being always positive quantities; neither can they be ignored because this would require very small size for the ΔS's and, ultimately, very large matrices. As mentioned before this behavior provides a first and necessary test of the correctness of "mode **B**" evaluations.

Combining modes A and B we end up with a system of 2N linear equations with unknowns $J_\varphi(\ell_c, \varphi_c)$ and $J_t(\ell_c, \varphi_c)$ the complex components of the surface current density induced on S at the centers of the chosen patches. Once these values are known it is simple to compute scattered field quantities on the basis of well-known surface integrals over S, particularly in the far field. An interesting question in this connection is when to switch from mode **A** to mode **B** and vice-versa. This question is closely related to the shape of ΔS (how elongated or "square" it is taken) and it is fully discussed in the concluding remarks of this paper, following numerical results for specific scatterers.

It is tempting to use Fourier series analysis over the interval $0 \leq \varphi \leq 2\pi$ for all quantities in (2), (3) and take advantage of their orthogonal properties. This procedure would reduce the two-dimensional surface integral equations into $2N_\ell$ one-dimensional ones over the interval $0 \leq \ell \leq L$; the latter are simpler and less time consuming to solve than the large-size matrix inversion required for the solution of the two-dimensional equations. However, it can be shown explicitly,

that such a procedure leads to divergent integrals, when $\ell' = \ell$; they arise from the three singular kernels $\partial G/\partial n(\ell, \ell', \varphi, \varphi')$, $\partial G/\rho\partial\varphi$, $\partial G/\partial t$ of (2), (3), that are split by Fourier analysis into 4 kernels $K_n(\ell, \ell')$ $(n = 1, 2, 3, 4)$, each expressed by certain Fourier integrals of known functions over the interval $0 \leq \varphi' \leq 2\pi$. Two of the latter diverge when $\ell' = \ell$ at both limits $\varphi' - \varphi = 0$ and 2π preventing application of this procedure. The reason is that an improper two-dimensional integral, even when convergent, cannot be split in the suggested way. Its convergence requires retaining both coordinates ℓ', φ' near the region of singularity, where $R \to 0$, and avoiding separation of the integrand into functions of ℓ' and φ' that are integrated sequentially [7].

In the following paragraphs the explicit formulas corresponding to the evaluation of the surface integrals in (2), (3) according to "mode **A**" and "mode **B**" are developed. They are then applied to the case of a sphere and the results for the current $\vec{J}(\vec{r})$ and the scattered field are compared with those of the classical Mie solution . Next the case of a parasitic dipole antenna of length 2h with hemispherical caps is considered and the results for the current I(z) are compared with those of King's approximate 3-term theory [10], which, for a limited range of antenna lengths, have been experimentally verified. These two cases serve as benchmark or test cases of our hybrid method and provide useful clues for its application in the most advantageous ways. Finally, the method is applied to other shapes, flat disks and cone-spheres, followed by a closing paragraph in which the numerical results are discussed and certain conclusions are drawn.

2. EVALUATION OF THE SURFACE "PATCH" INTEGRALS

We start by expressing the integrands of Maue's equations (2), (3) in terms of the new coordinates ℓ, ℓ', φ, φ', introduced for surfaces of revolution. If v denotes the angle between $\hat{t}$, $\hat{z}$ as in Figure 1, we have the obvious relations:

$$\frac{dz}{d\ell} = \cos v, \quad \frac{d\rho}{d\ell} = \sin v, \quad \left(\frac{d\rho}{d\ell}\right)^2 + \left(\frac{dz}{d\ell}\right)^2 = 1 \tag{4}$$

and the local unit vectors at $\vec{r}$ on S can be analyzed as follows:

$$\hat{n}(\vec{r}) = \cos\varphi \frac{dz}{d\ell}\hat{x} + \sin\varphi \frac{dz}{d\ell}\hat{y} - \frac{d\rho}{d\ell}\hat{z} \tag{5a}$$

$$\hat{t}(\vec{r}) = \cos\varphi \frac{d\rho}{d\ell}\hat{x} + \sin\varphi \frac{d\rho}{d\ell}\hat{y} + \frac{dz}{d\ell}\hat{z} \tag{5b}$$

$$\hat{\varphi}(\vec{r}) = -\sin\varphi\hat{x} + \cos\varphi\hat{y} \tag{5c}$$

Similar relations hold at $\vec{r}'$ in terms of ℓ', φ' and the same unit vectors $\hat{x}$, $\hat{y}$, $\hat{z}$. Noticing, also, that $\vec{J}(\vec{r}') \cdot \hat{n}(\vec{r}) = J_\varphi(\vec{r}')\hat{\varphi}(\vec{r}) \cdot \hat{n}(\vec{r}) + J_t(\vec{r}')\hat{t}(\vec{r}) \cdot \hat{n}(\vec{r})$ and the similar expressions for $\vec{J}(\vec{r}') \cdot \hat{\varphi}(\vec{r})$ and $\vec{J}(\vec{r}') \cdot \hat{t}(\vec{r})$ we easily end up with the general (and exact) expressions:

$$\begin{aligned}\hat{n}(\vec{r}) \cdot \vec{J}(\vec{r}') = &-J_\varphi(\ell', \varphi')\frac{dz}{d\ell}\sin(\varphi' - \varphi) \\ &- J_t(\ell', \varphi')\left[\frac{d\rho}{d\ell}\frac{dz}{d\ell'} - \frac{dz}{d\ell}\frac{d\rho}{d\ell'}\cos(\varphi' - \varphi)\right]\end{aligned} \tag{6a}$$

$$\hat{\varphi}(\vec{r}) \cdot \vec{J}(\vec{r}') = J_\varphi(\ell', \varphi')\cos(\varphi' - \varphi) + J_t(\ell', \varphi')\frac{d\rho}{d\ell}\sin(\varphi' - \varphi) \tag{6b}$$

$$\begin{aligned}\hat{t}(\vec{r}) \cdot \vec{J}(\vec{r}') = &-J_\varphi(\ell', \varphi')\frac{d\rho}{d\ell}\sin(\varphi' - \varphi) \\ &+ J_t(\ell', \varphi')\left[\frac{dz}{d\ell}\frac{dz}{d\ell'} + \frac{d\rho}{d\ell}\frac{d\rho}{d\ell'}\cos(\varphi' - \varphi)\right]\end{aligned} \tag{6c}$$

$$\begin{aligned}R^2 &= \Big[z(\ell') - z(\ell)\Big]^2 + \rho^2(\ell) + \rho^2(\ell') - 2\rho(\ell)\rho(\ell')\cos(\varphi' - \varphi) \\ &= \Big[z(\ell) - z(\ell')\Big]^2 + \Big[\rho(\ell') - \rho(\ell)\Big]^2 + 4\rho(\ell)\rho(\ell')\sin^2\left(\frac{\varphi' - \varphi}{2}\right)\end{aligned} \tag{7}$$

On the other hand from the well known relations for partial derivatives of the form:

$$-\frac{\partial G}{\partial n} = \frac{1 - jkR}{R^2}e^{jkR}\left[\frac{\partial R}{\partial x}(\hat{n} \cdot \hat{x}) + \frac{\partial R}{\partial y}(\hat{n} \cdot \hat{y}) + \frac{\partial R}{\partial z}(\hat{n} \cdot \hat{z})\right] \tag{8}$$

we end up again with the following (exact) expressions:

$$-\frac{\partial G}{\partial n} = \frac{1 - jkR}{R^3}e^{jkR}\left\{\begin{array}{c}\dfrac{dz}{d\ell}[\rho(\ell) - \rho(\ell')\cos(\varphi' - \varphi)] \\ + \dfrac{d\rho}{d\ell}[z(\ell') - z(\ell)]\end{array}\right\} \tag{9a}$$

$$\frac{\partial G}{\rho\partial\varphi} = \frac{1 - jkR}{R^3}e^{jkR}\rho(\ell')\sin(\varphi' - \varphi) \tag{9b}$$

$$\frac{\partial G}{\partial t} = -\frac{1 - jkR}{R^3}e^{jkR}\left\{\begin{array}{c}\dfrac{d\rho}{d\ell}[\rho(\ell) - \rho(\ell')\cos(\varphi' - \varphi)] \\ - \dfrac{dz}{d\ell}[z(\ell') - z(\ell)]\end{array}\right\} \tag{9c}$$

All these relations may now be substituted into (2), (3) and express Maue's equations in terms of the local coordinates ℓ, ℓ', φ, φ'. We next proceed with the explicit evaluation of the contribution of each patch $\Delta S'$ to the surface integrals appearing in (2), (3). The point of evaluation $\vec{r}$ may be any point on S interior or exterior to $\Delta S'$; it need not necessarily coincide with the center of another patch. When $\vec{r}'$ and $\vec{r}$ are far apart, i.e., when $R \gg d'$ and $kd' \ll 1$, we can take $R \cong R_c = \text{constant}$, $\vec{J}(\vec{r}') \cong \vec{J}(\vec{r}'_c) = \text{constant}$ and end up with trivial integrations. This way of evaluating the patch surface integrals was called previously "mode **A**" and, with the use of (6), yields

$$-\iint\limits_{\Delta S'} dS' \frac{\partial G}{\partial n} \begin{bmatrix} \hat{\varphi}(\vec{r}) \cdot \vec{J}(\vec{r}') \\ \hat{t}(\vec{r}) \cdot \vec{J}(\vec{r}') \end{bmatrix} \cong \begin{bmatrix} \hat{\varphi}(\vec{r}) \cdot \vec{J}(\vec{r}'_c) \\ \hat{t}(\vec{r}) \cdot \vec{J}(\vec{r}'_c) \end{bmatrix} \frac{1 - jkR_c}{R_c^3}$$
$$e^{jkR_c} \left\{ \frac{dz}{d\ell}[\rho(\ell) - \rho(\ell'_c)\cos(\varphi'_c - \varphi)] + \frac{d\rho}{d\ell}[z(\ell'_c) - z(\ell)] \right\} \Delta S' \tag{10}$$

$$\iint\limits_{\Delta S'} dS' \begin{bmatrix} \frac{\partial G}{\rho \partial \varphi} \\ \\ \frac{\partial G}{\partial t} \end{bmatrix} \left[\hat{n}(\vec{r}) \cdot \vec{J}(\vec{r}') \right] \cong \left[\hat{n}(\vec{r}) \cdot \vec{J}(\vec{r}'_c) \right] \frac{1 - jkR_c}{R_c^3}$$
$$e^{jkR_c} \begin{bmatrix} \rho(\ell'_c)\sin(\varphi'_c - \varphi) \\ -\frac{d\rho}{d\ell}[\rho(\ell) - \rho(\ell'_c)\cos(\varphi'_c - \varphi)] + \frac{dz}{d\ell}[z(\ell'_c) - z(\ell)] \end{bmatrix} \Delta S' \tag{11}$$

The expressions for $\hat{\varphi}(\vec{r}) \cdot \vec{J}(\vec{r}'_c)$, $\hat{t}(\vec{r}) \cdot \vec{J}(\vec{r}'_c)$ etc. and R_c follow from (6) and (7) if one uses ℓ'_c, φ'_c, the values at the center of $\Delta S'$, in place of ℓ', φ'.

When $\vec{r}$, $\vec{r}'$ are close to each other, so that $kR \ll 1$, then $\vec{r}$ belongs either to $\Delta S'$ (as $\vec{r}'$ does) or to a nearby patch. We may again substitute $\vec{J}(\vec{r}') \cong \vec{J}(\vec{r}'_c) = \text{constant}$, as long as $kd' \ll 1$, but, R now cannot be considered constant in the course of integration. For the self patch it even vanishes making the corresponding surface integrals improper. We may proceed in this case with an approximate analytical evaluation of the patch integrals if we expand the numerators and denominators of the integrands in (2), (3) in local Taylor series around the point $\vec{r}$, i.e., we use the leading terms in $\ell' - \ell$ and $\varphi' - \varphi$. Two subcases have to be considered: a) $\rho(\ell)$ and $\rho(\ell')$ are "large", i.e., the nearby points $\vec{r}$, $\vec{r}'$ are far from the axis of S. b) Both $\vec{r}$, $\vec{r}$ are near the axis of S, implying that $\rho(\ell)$ and $\rho(\ell')$ are comparable to

ℓ and ℓ'. If only one of them is near the axis, but, the other far from of it we return to the "mode **A**" case.

In the first case $\Delta S'$ has a "trapezoidal" shape and both $|\ell' - \ell|$ and $|\rho(\ell)(\varphi' - \varphi)|$ are of the same small order. Using the second form of (7), (6) and (9) we obtain the following first-order approximations:

$$\begin{aligned} \rho(\ell') - \rho(\ell) &= \frac{d\rho}{d\ell}(\ell' - \ell) + \frac{1}{2}\frac{d^2\rho}{d\ell^2}(\ell' - \ell)^2) + \ldots; \\ z(\ell') - z(\ell) &= \frac{dz}{d\ell}(\ell' - \ell) + \frac{1}{2}\frac{d^2z}{d\ell^2}(\ell' - \ell)^2) + \ldots; \end{aligned} \tag{12}$$

and with $\left(\frac{d\rho}{d\ell}\right)^2 + \left(\frac{dz}{d\ell}\right)^2 = 1$ from (4) we obtain:

$$\begin{aligned} R = |\vec{r}' - \vec{r}| &\cong \left\{ (\ell' - \ell)^2 + 4\rho^2(\ell)\sin^2\left(\frac{\varphi' - \varphi}{2}\right) + O[(\ell' - \ell)^3] \right\}^{1/2} \\ &\cong \left[(\ell' - \ell)^2 + \rho^2(\ell)(\varphi' - \varphi)^2 \right]^{1/2} \end{aligned} \tag{13}$$

$$\iint\limits_{\Delta S'} \frac{\partial G}{\partial n} dS' \cong -\rho(\ell) \iint\limits_{\Delta S'} d\ell' d\varphi' \frac{1}{R^3} \left[\begin{array}{l} 2\rho(\ell)\dfrac{dz}{d\ell}\sin^2\dfrac{\varphi' - \varphi}{2} + \\ \dfrac{1}{2}\left(\dfrac{d\rho}{d\ell}\dfrac{d^2z}{d\ell^2} - \dfrac{dz}{d\ell}\dfrac{d^2\rho}{d\ell^2}\right)(\ell' - \ell)^2 \end{array} \right] \tag{14}$$

$$\begin{aligned} &\iint\limits_{\Delta S'} \left[\hat{n}(\vec{r}) \cdot \vec{J}(\vec{r}') \right] \frac{\partial G}{\rho \partial \varphi} dS' \\ &\quad \cong -J_\varphi(\ell'_c, \varphi'_c)\frac{dz}{d\ell} \iint\limits_{\Delta S'} \frac{1}{R^3}\rho^2(\ell)\sin^2(\varphi' - \varphi) d\ell' d\varphi' \\ &\qquad - J_t(\ell'_c, \varphi'_c)\left[\frac{d\rho}{d\ell}\frac{d^2z}{d\ell^2} - \frac{dz}{d\ell}\frac{d^2\rho}{d\ell^2}\right] \iint\limits_{\Delta S'} \frac{\rho^2(\ell)\sin(\varphi' - \varphi)}{R^3}(\ell' - \ell) d\ell' d\varphi' \end{aligned} \tag{15}$$

$$\begin{aligned} &\iint\limits_{\Delta S'} \left[\hat{n}(\vec{r}) \cdot \vec{J}(\vec{r}') \right] \frac{\partial G}{\partial t} dS' \\ &\quad \cong -J_\varphi(\ell'_c, \varphi'_c)\frac{dz}{d\ell} \iint\limits_{\Delta S'} \frac{\sin(\varphi' - \varphi)}{R^3}(\ell' - \ell)\rho(\ell) d\ell' d\varphi' \\ &\qquad - J_t(\ell'_c, \varphi'_c)\left[\frac{d\rho}{d\ell}\frac{d^2z}{d\ell^2} - \frac{dz}{d\ell}\frac{d^2\rho}{d\ell^2}\right] \iint\limits_{\Delta S'} \frac{\rho(\ell)}{R^3}(\ell' - \ell)^2 d\ell' d\varphi' \end{aligned} \tag{16}$$

Substituting $\ell' - \ell = x$ and $2\rho(\ell)\sin\frac{\varphi'-\varphi}{2} = y$ we have further $y \cong \rho(\ell)(\varphi'-\varphi)$, $d\ell' = dx$, $dy = \rho(\ell)\cos\left(\frac{\varphi'-\varphi}{2}\right)d\varphi' \cong \rho(\ell)d\varphi'$ and $ydy = \rho^2(\ell)\sin(\varphi'-\varphi)d\varphi'$, the last being exact. Thus we get $R^2 \cong x^2 + y^2$ and

$$\begin{aligned}\iint\limits_{\Delta S'} \frac{\partial G}{\partial n} dS' \cong & -\frac{1}{2\rho(\ell)}\frac{dz}{d\ell}\int\limits_{x_-}^{x_+} dx \int\limits_{y_-}^{y_+} \frac{y^2 dy}{(x^2+y^2)^{3/2}} \\ & - \frac{1}{2}\left(\frac{d\rho}{d\ell}\frac{d^2z}{d\ell^2} - \frac{dz}{d\ell}\frac{d^2\rho}{d\ell^2}\right)\int\limits_{y_-}^{y_+} dy \int\limits_{x_-}^{x_+} \frac{x^2 dx}{(x^2+y^2)^{3/2}}\end{aligned} \tag{17}$$

$$\begin{aligned}\iint\limits_{\Delta S'} \left[\hat{n}(\vec{r})\cdot\vec{J}(\vec{r}')\right]\frac{\partial G}{\rho\partial\varphi} dS' \cong & -J_\varphi(\ell_c', \varphi_c')\frac{dz}{d\ell}\frac{1}{\rho(\ell)}\int\limits_{x_-}^{x_+} dx \int\limits_{y_-}^{y_+} \frac{y^2 dy}{(x^2+y^2)^{3/2}} \\ & - J_t(\ell_c', \varphi_c')\left(\frac{d\rho}{d\ell}\frac{d^2z}{d\ell^2} - \frac{dz}{d\ell}\frac{d^2\rho}{d\ell^2}\right)\int\limits_{x_-}^{x_+} x dx \int\limits_{y_-}^{y_+} \frac{ydy}{(x^2+y^2)^{3/2}}\end{aligned} \tag{18}$$

$$\begin{aligned}\iint\limits_{\Delta S'} \left[\hat{n}(\vec{r})\cdot\vec{J}(\vec{r}')\right]\frac{\partial G}{\partial t} dS' \cong & -J_\varphi(\ell_c', \varphi_c')\frac{dz}{d\ell}\frac{1}{\rho(\ell)}\int\limits_{x_-}^{x_+} x dx \int\limits_{y_-}^{y_+} \frac{ydy}{(x^2+y^2)^{3/2}} \\ & - J_t(\ell_c', \varphi_c')\left(\frac{d\rho}{d\ell}\frac{d^2z}{d\ell^2} - \frac{dz}{d\ell}\frac{d^2\rho}{d\ell^2}\right)\int\limits_{y_-}^{y_+} dy \int\limits_{x_-}^{x_+} \frac{x^2 dx}{(x^2+y^2)^{3/2}}\end{aligned} \tag{19}$$

where

$$x_\pm = \ell_c' - \ell \pm (\Delta\ell'/2), \qquad y_\pm = \rho(\ell)[\varphi_c' - \varphi \pm (\Delta\varphi'/2)] \tag{20}$$

Two types of integrals appear:

$$\begin{aligned}D(x_+, x_-; y_+, y_-) &= \int\limits_{x_-}^{x_+} x^2 dx \int\limits_{y_-}^{y_+} \frac{dy}{(x^2+y^2)^{3/2}} \\ &= (y_+)\ell n\frac{x_+ + \sqrt{x_+^2+y_+^2}}{x_- + \sqrt{x_-^2+y_+^2}} - (y_-)\ell n\frac{x_+ + \sqrt{x_+^2+y_-^2}}{x_- + \sqrt{x_-^2+y_-^2}}\end{aligned} \tag{21}$$

$$E(x_+,x_-;y_+,y_-)=\int_{x_-}^{x_+}xdx\int_{y_-}^{y_+}\frac{ydy}{(x^2+y^2)^{3/2}} \tag{22}$$
$$=-(x_+^2+y_+^2)^{1/2}+(x_-^2+y_+^2)^{1/2}+(x_+^2+y_-^2)^{1/2}$$
$$-(x_-^2+y_-^2)^{1/2}$$

It is easy at this point to verify that both these integrals vanish, when either $\Delta\varphi'=0$ or $\Delta\ell'=0$, i.e., when $\Delta S'=0$ either by letting $y_+=y_-$ or $x_+=x_-$, as seen from (20); and this happens for any value of ℓ, φ, i.e., for $\vec{r}$ either interior or exterior to $\Delta S'$. So, even for the self-patch, the integrals are convergent, in accordance with theory. The final formulas for "mode B" are:

$$\iint_{\Delta S'}\frac{\partial G}{\rho\partial\varphi}dS'\cong-\frac{1}{2\rho(\ell)}\frac{dz}{d\ell}D(y_+,y_-;x_+,x_-)$$
$$-\frac{1}{2}\left(\frac{d\rho}{d\ell}\frac{d^2z}{d\ell^2}-\frac{dz}{d\ell}\frac{d^2\rho}{d\ell^2}\right)D(x_+,x_-;y_+,y_-) \tag{23}$$
$$\iint_{\Delta S'}\left[\hat{n}(\vec{r})\cdot\vec{J}(\vec{r}')\right]\frac{\partial G}{\rho\partial\varphi}dS'\cong-J_\varphi(\ell_c',\varphi_c')\frac{dz}{d\ell}\frac{1}{\rho(\ell)}D(y_+,y_-;x_+,x_-)$$
$$-J_t(\ell_c',\varphi_c')\left(\frac{d\rho}{d\ell}\frac{d^2z}{d\ell^2}-\frac{dz}{d\ell}\frac{d^2\rho}{d\ell^2}\right)E(x_+,x_-;y_+,y_-) \tag{24}$$
$$\iint_{\Delta S'}\left[\hat{n}(\vec{r})\cdot\vec{J}(\vec{r}')\right]\frac{\partial G}{\partial t}dS'\cong-J_\varphi(\ell_c',\varphi_c')\frac{dz}{d\ell}\frac{1}{\rho(\ell)}E(x_+,x_-;y_+,y_-)$$
$$-J_t(\ell_c',\varphi_c')\left(\frac{d\rho}{d\ell}\frac{d^2z}{d\ell^2}-\frac{dz}{d\ell}\frac{d^2\rho}{d\ell^2}\right)D(x_+,x_-;y_+,y_-) \tag{25}$$

At the center of the self-patch $\ell=\ell_c'$, $\varphi=\varphi_c'$, $x_\pm=\pm\Delta\ell'/2$, $y_\pm=\pm\rho(\ell)\Delta\varphi'/2$ and

$$D(x_+,-x_+;y_+,-y_+)=4(y_+)\ell n\frac{x_++\sqrt{x_+^2+y_+^2}}{|y_+|}, \tag{26}$$
$$E(x_+,-x_+;y_+,-y_+)=0$$

Again $D=0$ either for $\Delta\varphi'=0$ or $\Delta\ell'=0$ and the integrals are convergent at the center of the self-patch, $\vec{r}=\vec{r}_c'$.

At the bottom and top of S we choose small "cyclical" patches of radius c around $\ell'_c = 0, L$. Now $\rho(\ell') \cong \ell'$ and the previous analysis fails. Also, φ'_c, J_φ, J_t cannot be defined at these points. $\vec{J}(\ell = 0, L)$ may now be defined via its J_x and J_y components, with the plane xz or $\varphi = 0°$, taken as the plane of incidence. For a given meridian plane φ we can define J_φ, J_t at $\ell = 0, L$ through the obvious relations (see Figure 2).

$$\begin{aligned} J_\varphi(\ell = 0, L) &= -J_x \sin\varphi + J_y \cos\varphi \\ J_t(\ell = 0, L) &= J_x \cos\varphi + J_y \sin\varphi \\ J_x &= -J_\varphi \sin\varphi + J_t \cos\varphi \\ J_y &= J_\varphi \cos\varphi + J_t \sin\varphi \end{aligned} \tag{27}$$

When $\vec{r}$ is away from $\vec{r}'_c(\ell'_c = 0, L)$, the "mode **A**" formulas (10), (11) remained unchanged and can be used. When $\vec{r}$ is in the interior or near exterior of these two cyclical patches their contribution needs separate evaluation. Elliptic integrals appear in the general case, which is left for a subsequent paper. Here we restrict ourselves to the self-patch contribution at the center of the cyclical patches, i.e., when $\vec{r} = \vec{r}'_c(\ell = \ell'_c = 0, L)$, taking into account the fact that for the solution of Maue's equation only values at the center of patches are involved. The contribution of the cyclical patches at the centers of its adjacent patches is here evaluated using mode **A** formulas; there is sufficient numerical evidence that this assumption, by which more complicated integrals are avoided, is quite sufficient for practical purposes and will be further discussed later on. Now, with $\vec{r} = \vec{r}'_c$ and $\ell = \ell'_c = 0, L$ we have $\rho(\ell) = 0$, $\frac{dz}{d\ell} = 0$ and

$$\left(\frac{d\rho}{d\ell}\right)_{\ell=0} = 1, \quad \rho(\ell') = \ell', \quad z(\ell') = \frac{1}{2}\frac{d^2 z}{d\ell^2}\ell'^2$$

$$R \cong \ell', \quad \frac{dz}{d\ell'} \cong \frac{d^2 z}{d\ell^2}\ell' \text{ for } \ell = 0 \tag{28}$$

$$\left(\frac{d\rho}{d\ell}\right)_{\ell=L} = -1, \quad \rho(\ell') = L - \ell',$$

$$z(\ell') - z(L) = \frac{1}{2}\left(\frac{d^2 z}{d\ell^2}\right)_{\ell=L}(L - \ell')^2,$$

$$R \cong L - \ell', \quad \frac{dz}{d\ell'} \cong \frac{d^2 z}{d\ell^2}(\ell' - L) \text{ for } \ell = L \tag{29}$$

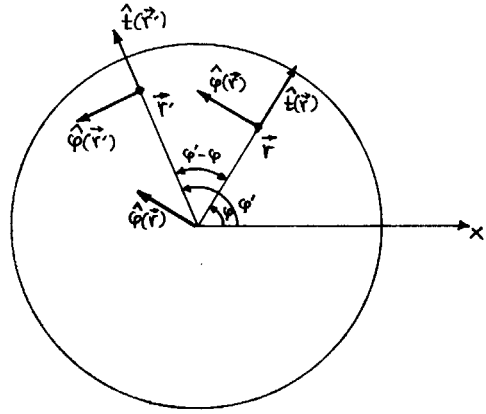

Figure 2. Unit vector analysis in the cyclical patch around $\ell = 0$.

Returning to (9) we have, in the first case $\ell = \ell'_c = 0$:

$$-\frac{\partial G}{\partial n} \cong \frac{1}{2}\frac{d^2 z}{d\ell^2}\frac{1}{\ell'}; \quad \frac{\partial G}{\rho \partial \varphi} \cong \frac{\sin(\varphi' - \varphi)}{\ell'^2}; \quad \frac{\partial G}{\partial t} \cong \frac{\cos(\varphi' - \varphi)}{\ell'^2} \tag{30}$$

We, also, set again $\hat{\varphi}(\vec{r}) \cdot \vec{J}(\vec{r}') \cong \hat{\varphi}(\vec{r}) \cdot \vec{J}(\vec{r}) = J_\varphi(\ell = 0)$ and $\hat{t}(\vec{r}) \cdot \vec{J}(\vec{r}') \cong \hat{t}(\vec{r}) \cdot \vec{J}(\vec{r}) = J_t(\ell = 0)$, whereas from (5b) and (6a) $\hat{n}(\vec{r}) \cdot \vec{J}(\vec{r}') \cong -\hat{z} \cdot \hat{t}(\vec{r}')J_t(\vec{r}') = -\frac{dz}{d\ell'}J_t(\vec{r}') \cong -\frac{d^2 z}{d\ell^2}\ell'[\vec{J}(\ell = 0) \cdot \hat{t}(\vec{r}')]$. The approximation $J_t(\vec{r}') \cong \vec{J}(\ell = 0) \cdot \hat{t}(\vec{r})$ is obvious, because $\vec{r}'$ is near $\vec{r}(\ell = 0)$; analyzing further $\vec{J}(\ell = 0) = J_\varphi(\ell = 0)\hat{\varphi}(\vec{r}) + J_t(\ell = 0)\hat{t}(\vec{r})$ as seen from Figure 2, and using (5bc) we get $\hat{t}(\vec{r}) \cdot \hat{t}(\vec{r}') \cong \cos(\varphi' - \varphi)$, $\hat{\varphi}(\vec{r}) \cdot \hat{t}(\vec{r}') \cong \sin(\varphi' - \varphi)$ and finally

$$\hat{n}(\vec{r}) \cdot \vec{J}(\vec{r}') = -\frac{d^2 z}{d\ell^2}\ell'[J_\varphi(\ell = 0)\sin(\varphi' - \varphi) + J_t(\ell = 0)\cos(\varphi' - \varphi)] \tag{31}$$

Substitution in (2), (3) yields

$$\iint\limits_{\Delta S'} dS' \left\{ -\frac{\partial G}{\partial n}\begin{bmatrix} \hat{\varphi}(\vec{r}) \cdot \vec{J}(\vec{r}') \\ \hat{t}(\vec{r}) \cdot \vec{J}(\vec{r}') \end{bmatrix} + \begin{bmatrix} \frac{\partial G}{\rho \partial \varphi} \\ \\ \frac{\partial G}{\partial t} \end{bmatrix} \left[\hat{n}(\vec{r}) \cdot \vec{J}(\vec{r}')\right] \right\}$$

$$= \int\limits_0^{2\pi} \int\limits_0^c \ell' d\ell' d\varphi' \left\{ \frac{1}{2}\frac{d^2 z}{d\ell^2}\frac{1}{\ell'}\begin{bmatrix} J_\varphi(\ell = 0) \\ J_t(\ell = 0) \end{bmatrix} \right.$$

$$- \begin{bmatrix} \sin(\varphi' - \varphi) \\ \cos(\varphi' - \varphi) \end{bmatrix} \frac{1}{\ell'^2} \frac{d^2 z}{d\ell^2} \ell' \begin{bmatrix} J_\varphi(\ell = 0) \sin(\varphi' - \varphi) \\ + J_t(\ell = 0) \cos(\varphi' - \varphi) \end{bmatrix} \Bigg\}$$

$$= 2\pi c \frac{1}{2} \frac{d^2 z}{d\ell^2} \begin{bmatrix} J_\varphi(\ell = 0) \\ J_t(\ell = 0) \end{bmatrix} - \frac{d^2 z}{d\ell^2} c\pi \begin{bmatrix} J_\varphi(\ell = 0) \\ J_t(\ell = 0) \end{bmatrix} = 0 \qquad (32)$$

A similar analysis around the top point $\ell = L$ gives the same result, 0. This completes the self-patch contribution to the surface integrals in (2), (3), for the cyclical bottom and top patches of radius c, using mode **B**.

3. APPLICATION TO SPECIFIC SCATTERERS

3.1 Perfectly Conducting Spheres

The method was first applied to perfectly conducting spheres, where the classical Mie solution provides a sound base for comparison of results obtained by various approaches. We have been able to reproduce with high accuracy a variety of plots, found in the literature [11–15], for the current density $\vec{J}$ induced on the sphere and for the scattered field. In general, the accuracy for the scattered field, when compared with the corresponding exact Mie result, is much better than for $\vec{J}$; this is a well known fact, due to the insensitivity of the far scattered field to small changes in $\vec{J}$. Therefore, accuracy is tested by comparing values of $\vec{J}$ rather than far-field ones. Also, for larger spheres (larger $k\alpha$) all methods, including Mie's, require much more computational labour and increased numerical (decimal) accuracy. It suffices to compare and test results of any method near the upper limit of the so-called resonance region, beyond which, for each scatterer , the physical optics approximation takes over. With these remarks in mind we present in Figures 3, 4 results for the normalized (per unit H^{inc}) amplitudes $|J_t|$, $|J_\varphi|$ of the components of the surface current density on the sphere by our method and by Mie's exact solution for $k\alpha = 20$, the upper limit of the resonance region, as defined on page 147 of [12]. We selected the meridian plane $\varphi = 45^\circ$ for which both J_t and J_φ components are present, whereas $J_\varphi = 0$ for $\varphi = 0^\circ$. The total number of patches, $N = 1542$, is indicated in both figures 3, 4 and the division of the spherical surface into them, near the bottom patch $\ell = 0$, in Figure 5. Shown, also, are the values N_φ, for each ring surface $\ell_n \leq \ell \leq \ell_n + \Delta\ell_n$, the $\Delta\ell_n$'s and their total number N_ℓ. When $\vec{J}$

is to be evaluated at a predetermined meridian $\varphi = \varphi_0$ on S, and in order to avoid interpolation, we turn slightly the ring surfaces so that all middle points φ_c of the patches containing the value $\varphi = \varphi_0$ are aligned on $\varphi = \varphi_0$ (i.e., $\varphi_c = \varphi_0$). This is indicated in Figure 5; it is not necessary for field evaluations at $\varphi = \varphi_0$. For well known reasons [16] elongated patches should be avoided, and shapes as much "square" as possible must be chosen. Another representative figure is the average number of divisions per wavelength, $\lambda/(\Delta S)^{1/2} = (N\pi)^{1/2}/k\alpha$, which for $N = 1542$ and $k\alpha = 20$ amounts to 3.48, a rather low figure, if compared with other numerical approaches. Despite this, the agreement with the exact Mie results is excellent, even in the shadow region (around $\theta = 180^\circ$ or $\ell = 0$) where the expected standing wave pattern for $|J_t|$ prevails. We attribute this behavior and accuracy of the hybrid method to the analytic evaluation of the most important self-patch contribution to the integrals, in contrast with other numerical methods, based on so-called "principal value" approaches [6, 13], which in effect ignore the self-patch contribution; this, in turn, requires smaller patch sizes and larger matrices than ours. For instance, a figure of 6 divisions per wavelength, as suggested on page 104 of [12], leads to $N = 4584$, three times larger than our matrix size.

To obtain the results for spheres (and the other shapes that follow) "mode B" was used for the self-patch only, while for exterior patches, even for its adjacent ones, "mode A" was applied. The results thus obtained were as good (even a little better) as those obtained with "mode B" extended to patches adjacent to the self-patch and "mode A" to all others beyond its immediate neighbors. The qualification "even a little better" was based, in the case of spheres, on comparisons with the exact Mie results. An explanation for this result, related to a lack of reciprocity of results based on "mode B", was suggested by Professor T. T. Wu of Harvard University; we return to this point in more detail later on, in the Conclusions.

Finally, in Figure 6 the normalized scattering cross-section $\sigma(\vartheta)/\pi\alpha^2$ [12] is shown in the meridian plane $\varphi = 0^\circ$. It can be compared with the corresponding plot on page 152 of [12] based on Mie's solution, which is repeated in Figure 6 for comparison. The agreement in the forward directions is excellent, while in the backward ones it varies around the (normalized) value of 1, i.e., the optical limit.

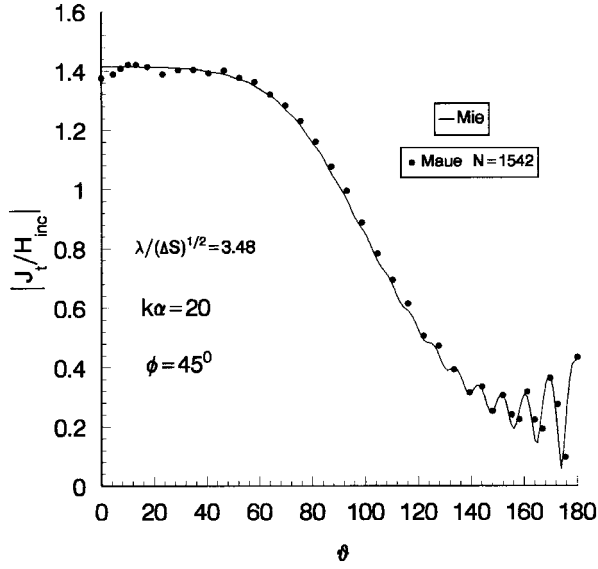

Figure 3. Normalized amplitude of the surface current density component $|J_t|$ vs ϑ for $\varphi = 45^\circ$ and for a sphere with $k\alpha = 20$.

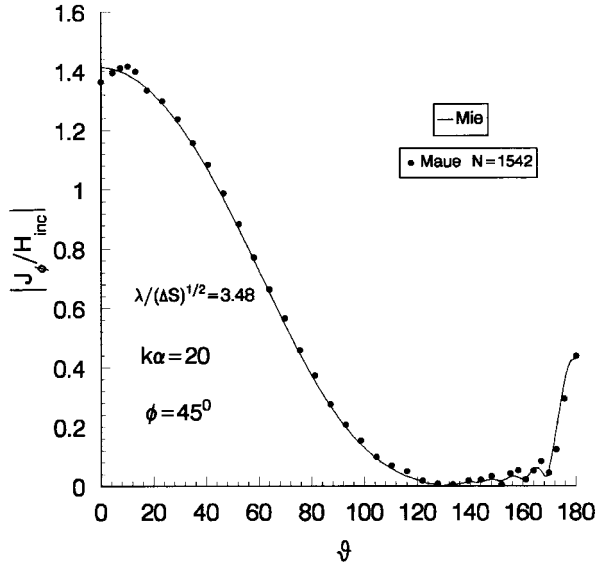

Figure 4. Same as in Figure 3 for $|J_\varphi|$.

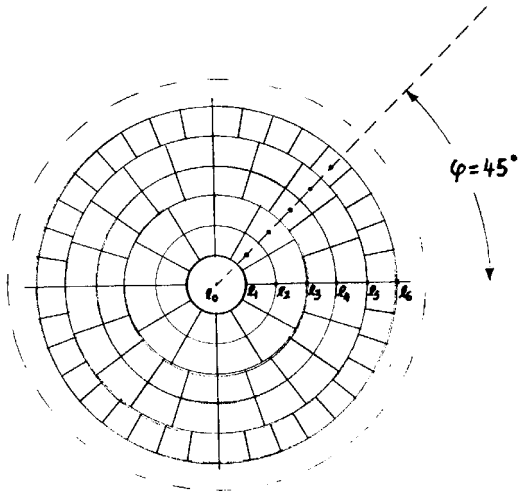

$\Delta\ell = (\pi\alpha - 2\ell_1)/30$

$\ell_0 = 0$	
$\ell_1 = .0166\pi\alpha$	N_φ=1
$\ell_2 = \ell_1 + \Delta\ell/2$	N_φ=12
$\ell_3 = \ell_2 + \Delta\ell/2$	N_φ=12
$\ell_4 = \ell_3 + \Delta\ell/2$	N_φ=20
$\ell_5 = \ell_4 + \Delta\ell/2$	N_φ=20
$\ell_6 = \ell_5 + \Delta\ell/2$	N_φ=36
$\ell_7 = \ell_6 + \Delta\ell/2$	N_φ=36
$\ell_8 = \ell_7 + \Delta\ell/2$	N_φ=52
$\ell_9 = \ell_8 + \Delta\ell/2$	N_φ=52
$\ell_{10} = \ell_9 + 2\Delta\ell/3$	N_φ=52
$\ell_{11} = \ell_{10} + 2\Delta\ell/3$	N_φ=52
$\ell_{12} = \ell_{11} + 2\Delta\ell/3$	N_φ=52
$\ell_{13} = \ell_{12} + \Delta\ell$	N_φ=36
$\ell_{14} = \ell_{13} + \Delta\ell$	N_φ=44
$\ell_{15} = \ell_{14} + \Delta\ell$	N_φ=52
$\ell_{16} = \ell_{15} + \Delta\ell$	N_φ=52
$\ell_{17} = \ell_{16} + \Delta\ell$	N_φ=60
$\ell_{18} = \ell_{17} + \Delta\ell$	N_φ=60
$\ell_{19} = \ell_{18} + \Delta\ell$	N_φ=60
$\ell_{20} = \ell_{19} + \Delta\ell$	N_φ=60
$\ell_{21} = \ell_{20} + \Delta\ell$	N_φ=60
$\ell_{22} = \ell_{21} + \Delta\ell$	N_φ=60
$\ell_{23} = \ell_{22} + \Delta\ell$	N_φ=60
$\ell_{24} = \ell_{23} + \Delta\ell$	N_φ=60
$\ell_{25} = \ell_{24} + \Delta\ell$	N_φ=60
$\ell_{26} = \ell_{25} + \Delta\ell$	N_φ=60
$\ell_{27} = \ell_{26} + \Delta\ell$	N_φ=52
$\ell_{28} = \ell_{27} + \Delta\ell$	N_φ=52
$\ell_{29} = \ell_{28} + \Delta\ell$	N_φ=44
$\ell_{30} = \ell_{29} + \Delta\ell$	N_φ=36
$\ell_{31} = \ell_{30} + \Delta\ell$	N_φ=36
$\ell_{32} = \ell_{31} + \Delta\ell$	N_φ=28
$\ell_{33} = \ell_{32} + \Delta\ell$	N_φ=28
$\ell_{34} = \ell_{33} + \Delta\ell$	N_φ=20
$\ell_{35} = \ell_{34} + \Delta\ell/2$	N_φ=20
$\ell_{36} = \ell_{35} + \Delta\ell/2$	N_φ=20
$\ell_{37} = \ell_{36} + \Delta\ell/2$	N_φ=12
$\ell_{38} = \ell_{37} + \Delta\ell/2$	N_φ=12
$\ell_{39} = \ell_{38} + .0166\pi\alpha$	N_φ=1

Figure 5. Segmentation of spherical surface around the bottom cyclical patch $(\ell = 0)$ and number of patches N_φ per ring.

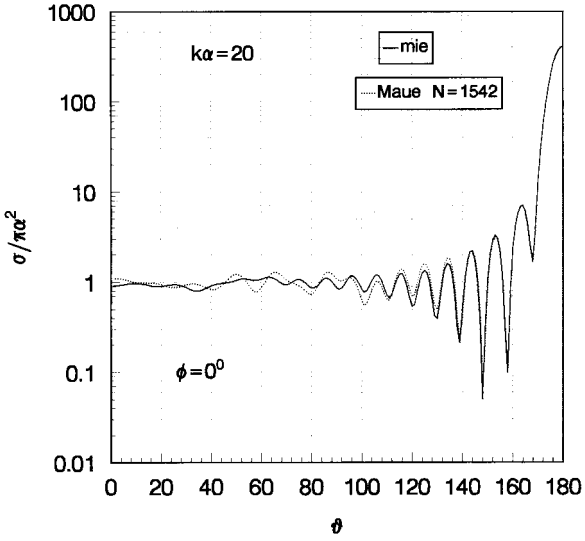

Figure 6. Normalized scattering cross-section of sphere with $k\alpha = 20$ at $\varphi = 0^\circ$.

Many more plots for spheres found in the literature were reproduced using our method with high accuracy and reasonable matrix sizes; they are not shown in this paper, since they correspond to $k\alpha < 20$; they can be found in A. Magoulas's Ph.D. thesis [17]. As an indication we simply mention that the well-known Mie plot for the back scattering cross-section of the sphere versus $k\alpha$ was very well approximated, up to $k\alpha \leq 3.5$, with $N = 612$ patches; higher N was necessary for $k\alpha > 3.5$. Also, owning to its "peculiar" shape we evaluated by our method (for $\varphi = 0^\circ$ and 90° and $k\alpha = 2.8$) the far field intensity as a function of ϑ included in Figure 4.52, page 163, of Kerker [11]; our result turned out to be identical to Mie's result in [11].

3.2 Thin Dipole Scatterer

As mentioned in the Introduction, this case was considered next as a test, owing to the experimentally verified results for the current distribution $I_z(z)$ based on King's approximate three-term theory [10]. This theory applies to both driven and parasitic (short-circuited) tubular thin dipoles of length $2h$ in the range of h/λ - values between

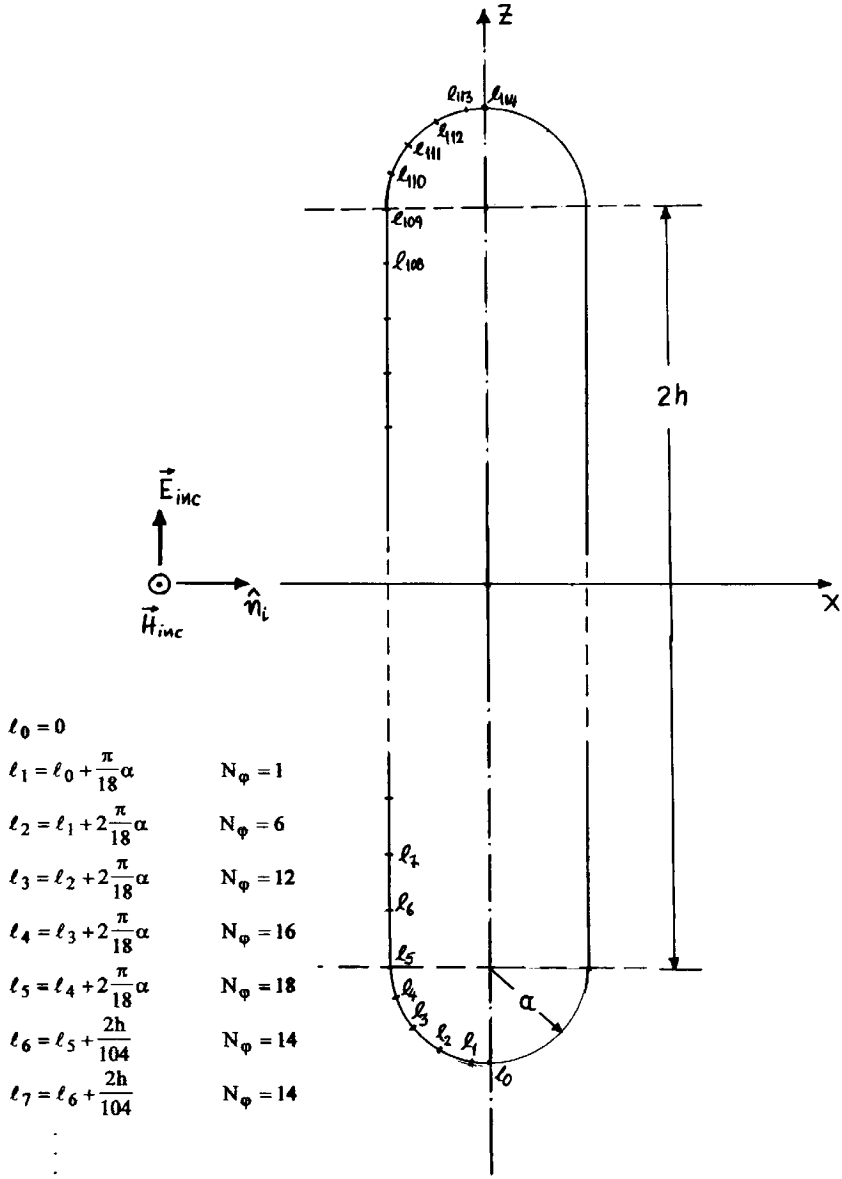

Figure 7. The thin dipole scatterer with hemispherical caps.

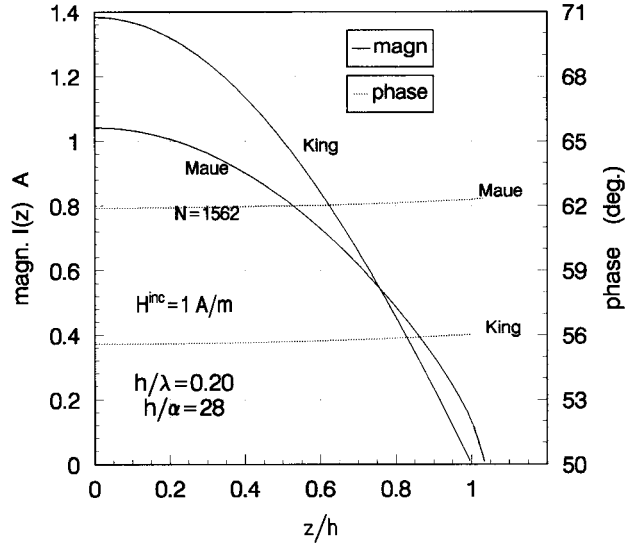

Figure 8. Amplitude and phase of total current $I_z(z)$ of a dipole with $h/\alpha = 28$, $h/\lambda = 0.20$.

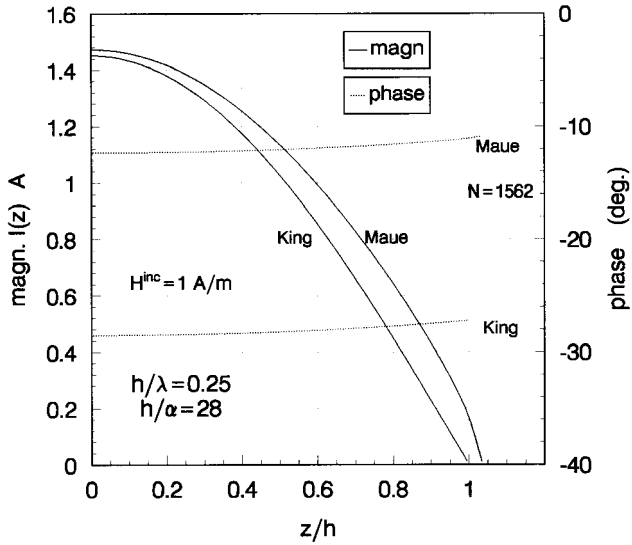

Figure 9. Same as Figure 8, but for $h/\lambda = 0.25$.

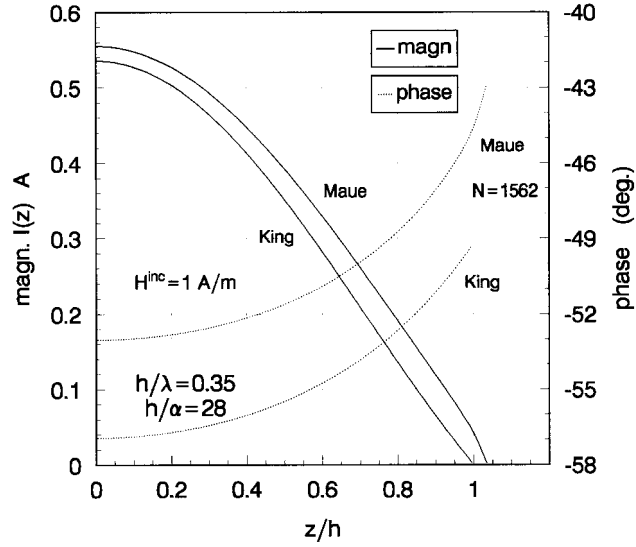

Figure 10. Same as Figure 8, but for $h/\lambda = 0.35$.

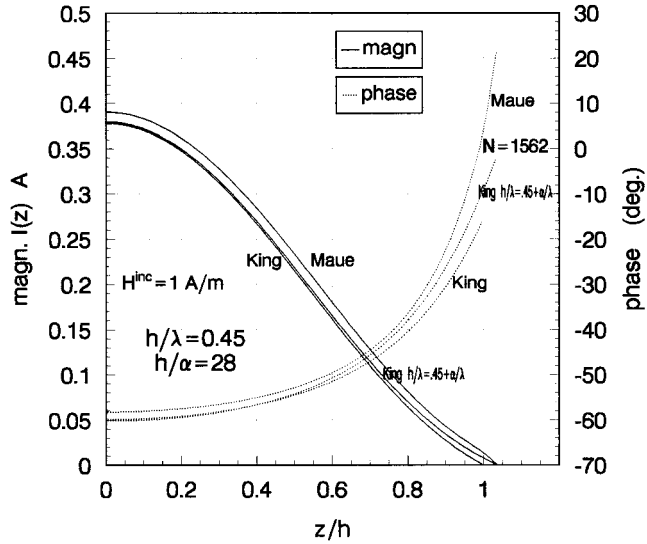

Figure 11. Same as Figure 8, but for $h/\lambda = 0.45 - 0.45 + \frac{\alpha}{\lambda}$.

about 0.20 to 0.50. In our case the scatterer is terminated in hemispherical caps of radius α, the antenna radius, to avoid edges, as shown in Figure 7; its total length is $2h+2\alpha$. In Figures 8–11 we plot the amplitude and phase of the current $I_z(z)$ induced on thin dipoles with $h/\alpha = 28$ and $h/\lambda = 0.20,\ 0.25,\ 0.35,\ 0.45$ In the last case King's result is evaluated for lengths $h/\lambda = 0.45$ and $0.45+\alpha/\lambda$.The total current $I_z(z)$ in the upper spherical cap is evaluated through the z- projection J_{tz} of the current density component J_t at a distance $\rho = \alpha\cos(\ell_1/\alpha)$ from the axis, where ℓ_1 is arc length measured on the semicircular path from its junction with the cylindrical surface of the dipole; similarly for the bottom cap. The number of patches, shown in the Figures, varies around $N = 1500$, owing to the small radius of curvature α of the cylindrical surface and the necessity of avoiding elongated patches. For these reasons, it is obvious, that our method is not the best for evaluating $I_z(z)$, but, as already explained, the case was considered for comparison with experimentally verified results. Taking into account that King's three-term theory provides an approximation to $I_z(z)$ we observe that the agreement with our result is very good, particularly for the amplitude $|I_z(z)|$. A difference of $5^\circ - 20^\circ$ in the phase of $I_z(z)$ is not so important if one considers $I_z(z)$ as a phasor and, in addition, for lower h/λ values, the three-term theory can be further approximated by the two-term theory [10], which predicts a constant phase for $I_z(z)$. Our results verify this prediction for $h/\lambda = 0.20,\ 0.25$, yielding an almost constant phase for $I_z(z)$.

Finally, thicker dipoles, $h/\alpha = 10$, were considered. Results from the three-term approximation are not expected to be reliable any more; this is born out by our method which shows considerable discrepancy for the shorter lengths $h/\lambda = 0.20$ to 0.30; our results are to be considered as the true ones in this case. For lengths around $h/\lambda = 0.40$ to 0.45, however, the agreement continues to be good. This implies that for thicker dipoles the three-term theory is not invalidated, but, its range of applicability is shortened around the value $h/\lambda = 0.40$.

3.3 Flat Discs

The next scatterer-shape that we considered is a flat disc of radius α thickness $2r_1$, where r_1 is the radius of the semi-toroidal surface by which the disc is closed around its periphery with continuous normal to avoid edges, as shown in Figure 12. This shape was chosen in order

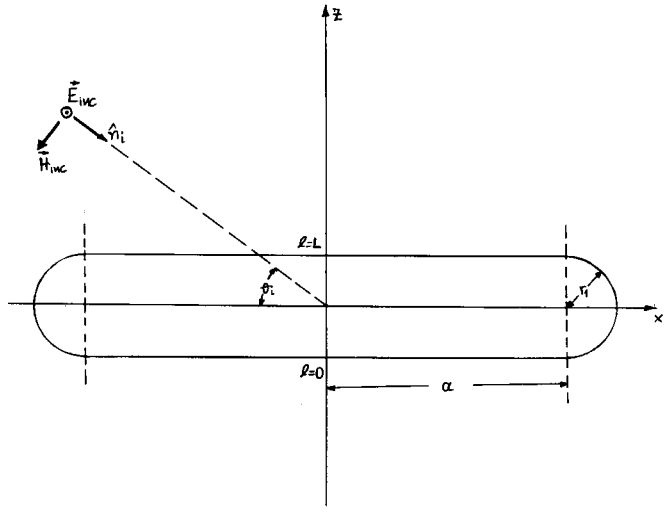

Figure 12. The flat disc without edges.

to study the edge-behavior of the scatterer as r_1/α is decreased, for very thin discs; another reason is the fact that many matrix elements evaluated from (10)–(11) or (23)–(25) vanish, owing to the flat surfaces of the disc. The resulting matrix is sparse and so its inversion may be expedited.

In Figure 13 the normalized amplitudes $|J_t/H^{\rm inc}|$ and $|J_\varphi/H^{\rm inc}|$ of the surface current density components are plotted versus ℓ/L for an incident wave with $\hat{n}_i$ and $\vec{E}^{\rm inc}$ parallel to the flat surface of the disc ($\theta_i = 0^\circ$, grazing incidence) for a disc with $\alpha/\lambda = 1$ and $\alpha/r_1 = 10$. The number of patches N and the corresponding average number of divisions per wavelength $\lambda/(\Delta S)^{1/2}$ are 1090 - 11.4 and 730 - 9.33. The meridian planes are at $\varphi = 0^\circ$, 180° (where $J_t = 0$) and $\varphi = 90^\circ$ (where both J_φ , $J_t \neq 0$). For this polarization $\vec{E}^{\rm inc}$ is parallel to the edge at $\varphi = 0^\circ$, 180° and the effect on $|J_\varphi|$, i.e., the edge behavior, is pronounced; even more so for thinner discs with $\alpha/r_1 = 20$, as seen in Figure 14 ; here N is further increased to 1398 because the edge is sharper. The plots differ little between $N = 730$ and 1090, apart from the edge region $(\ell/L \cong 0.5)$, where a sharper, and presumably more accurate, representation of the edge behavior is obtained with $N = 1090$, or 1398, patches. In Figure 13 we, also, added the plot of $|J_\varphi/H^{\rm inc}|$ at the mid-plane $\ell = L/2$ for $-180^\circ \leq \varphi \leq 180^\circ$ (where $J_t = 0$). The expected standing-wave pattern for $|J|$ is

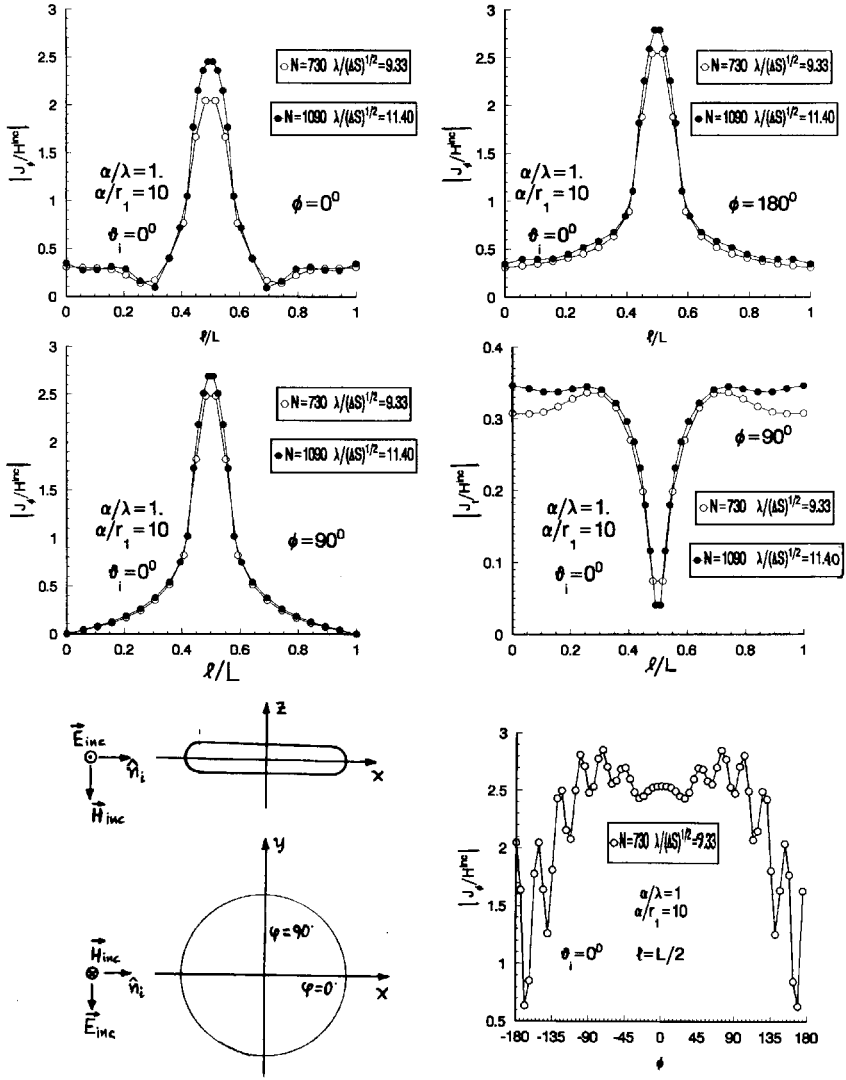

Figure 13. Normalized amplitudes of surface current density components $|J_t/H^{\rm inc}|$ and $|J_\varphi/H^{\rm inc}|$ vs ℓ/L on a disc with $\alpha/\lambda = 1$, $\alpha/r_1 = 10$, for grazing incidence $(\vartheta_i = 0°)$, for $\varphi = 0°, 180°$ (where $J_t = 0$) and $90°$. Also for the mid-plane $\ell = L/2$ versus φ (where $J_t = 0$). The plots for $N = 730$ and 1090 are superimposed.

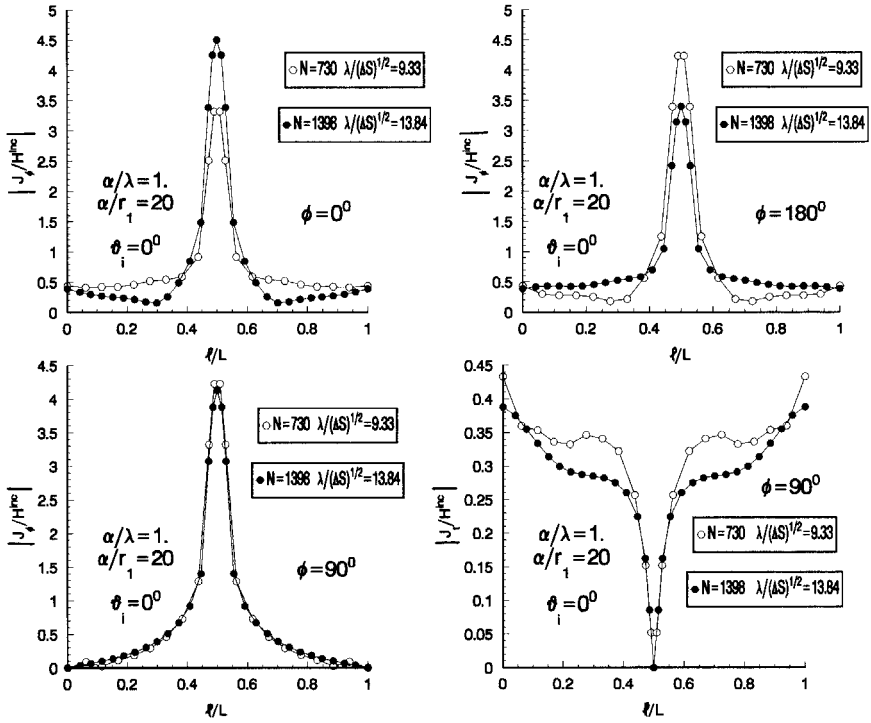

Figure 14. Same as Figure 13, but for $\alpha/r_1 = 20$ and $N = 730$ and 1398; the plot at the mid-plane $\ell = L/2$ is omitted here.

obvious from the plot. Figure 15 shows similar results with $\vartheta_i = 90°$ (incidence along the axis of the disc) and for $\varphi = 0°$ (where $J_t = 0$) and $\varphi = 90°$ (where $J_\varphi = 0$). In the shadow region ($0 \le \ell/L \le 0.5$) the current density is quite smaller than in the illuminated side, as expected, whereas J_t exhibits the standing wave behavior around $\ell = 0$, observed for spheres. Similar observations can be made, with a more pronounced standing wave pattern for J_t, in Figure 16, which correspond to a larger disc, $\alpha/\lambda = 2$, again for incidence along the axis. In Figure 17 $\alpha/\lambda = 1$, $\alpha/r_1 = 10$ and $\vec{E}^{\text{inc}}$ is again parallel to the disc, but the incidence is oblique at $\vartheta_i = 60°$, as shown. For $\varphi = 0°,\ 180°$ $J_t = 0$. In the shadow region $|\vec{J}|$ is quite smaller than in the illuminated side except for J_φ for $\varphi = 90°$, which is here the smaller component anyway and is affected by the edge.

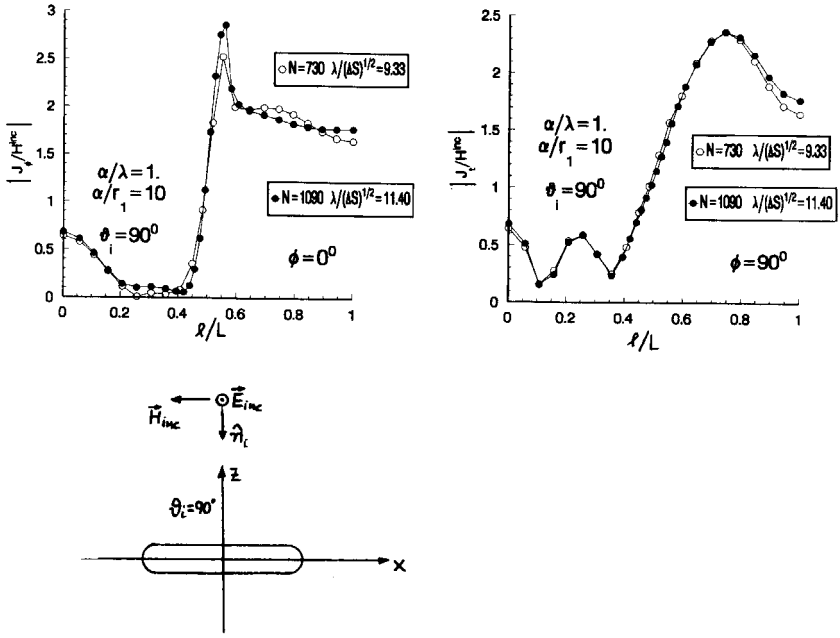

Figure 15. Same as Figure 13, but for normal incidence.

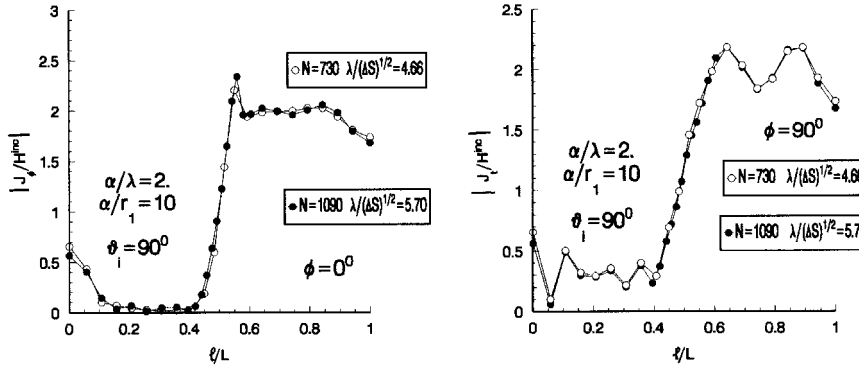

Figure 16. Same as Figure 15, but for a larger disc $\alpha/\lambda = 2$.

Finally, the scattered field pattern for a disc with $\alpha/\lambda = 1$, $\alpha/r_1 = 10$ and $\vartheta_i = 60^\circ$ is shown in Figure 18. The scattered field is large in the forward direction $\vartheta_f = 150^\circ$ ($\varphi_f = 0^\circ$) as well as in the reflected one $\vartheta_r = 30^\circ$ ($\varphi_r = 0^\circ$). Many more far field plots have been obtained, as well as current density and field plots for the other polarization, with $\vec{H}^{\text{inc}}$ parallel to the disc. Since they do not add much to the observations already made, these plots are omitted here to save space; they can be found in [17].

3.4 Sphere-cone-sphere

Another shape that is frequently investigated in the literature is the cone-sphere [12–14]. Here the tip is replaced by a small sphere of radius r_2 to avoid the edge, as shown in Figure 19. Most of the published results in cone-spheres are concerned with the scattered field. Rarely can one find plots for the surface current density. Two such plots are given on pages 217–218, Figure 4.15 of [13]. They refer to a cone-sphere with a 20 degree included angle and $k\alpha = 1.26$, α being the sphere radius. $|J_t/H^{\text{inc}}|$ and $|J_\varphi/H^{\text{inc}}|$ are plotted for both tip-end and sphere-end incidence along the axis; these current density components are evaluated by two methods: a Magnetic Field Integral Equation (MFIE) program, using uniform azimuthal segmentation and variable-width segments along the cone axis providing equal area patches on the cone, and an Electric Field Integral Equation for rotationally symmetric bodies based on Mautz and Harrington's method [14] with $n = 30$ equally spaced samples along the cone-sphere surface. Although for $|J_t|$ the results of the two approaches agree well, for $|J_\varphi|$ they differ significantly [13], with those of the first approach (MFIE) considered as closer to the true ones. In spite of this discrepancy, it is mentioned in [13], that "good agreement is observed in the bistatic scattering patterns, demonstrating the stationary property of the scattered field dependence on the current distribution". We reproduced these results with our method substituting the cone tip by a small sphere of radius $r_2 = r_1/16$, where $r_1 = \alpha$ is the radius of the large sphere (the base opposite the tip), as shown in Figures 20, 21. The surface was divided into $N = 546$ and 1194 patches for sphere-end and end tip-end incidence (Figure 20). The higher figure $N = 1194$ was tried to obtain a better picture of the current density behavior near the tip; away from it the plots for either 546 or 1194 patches coincide; near the tip the main difference is observed for $|J_t/H^{\text{inc}}|$ with values rising to about

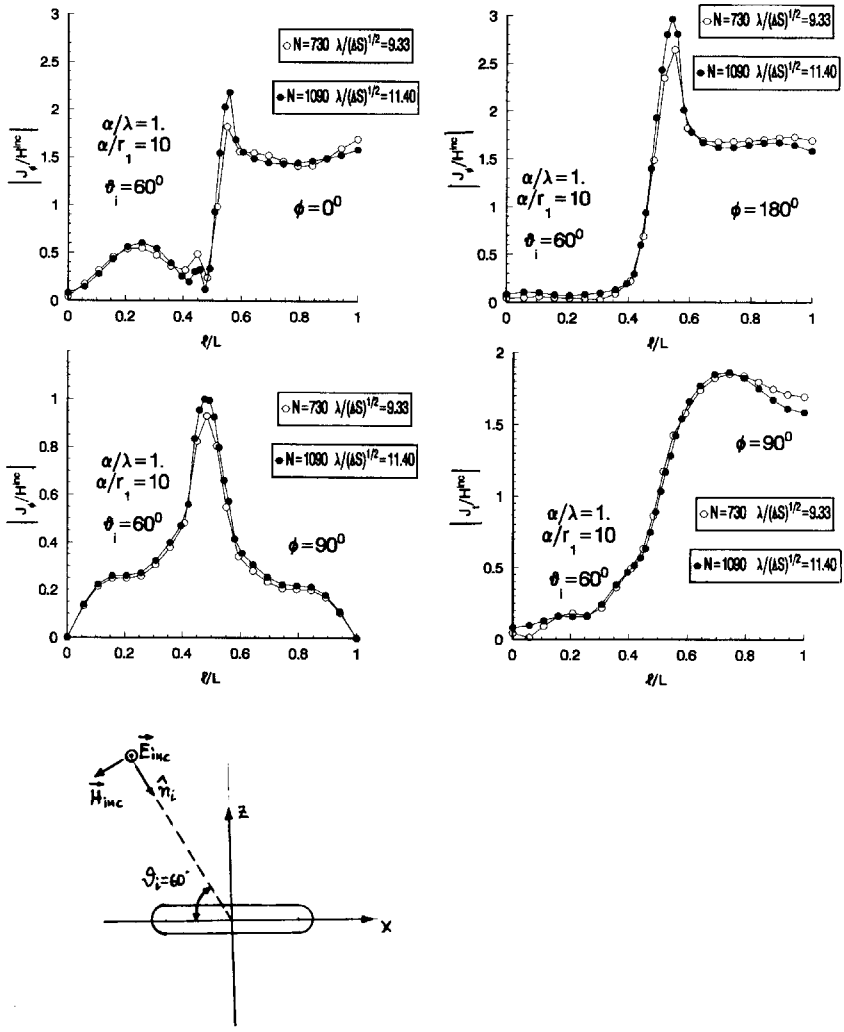

Figure 17. Same as Figure 13, but for oblique incidence $\vartheta_i = 60°$.

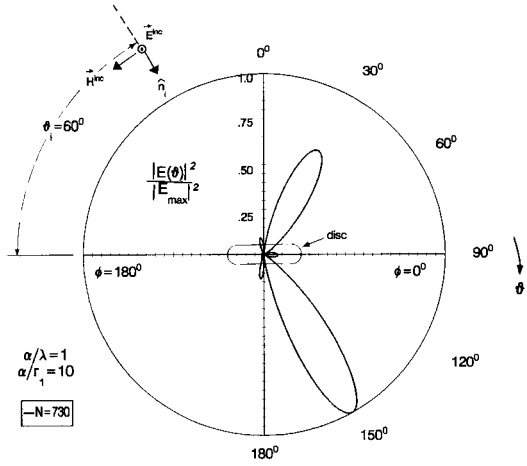

Figure 18. Relative scattered field intensity $|E(\vartheta)|^2$ for $\varphi = 0°, 180°$, $\vartheta_i = 60°$ of a disc with $\alpha/\lambda = 1$, $\alpha/r_1 = 10$.

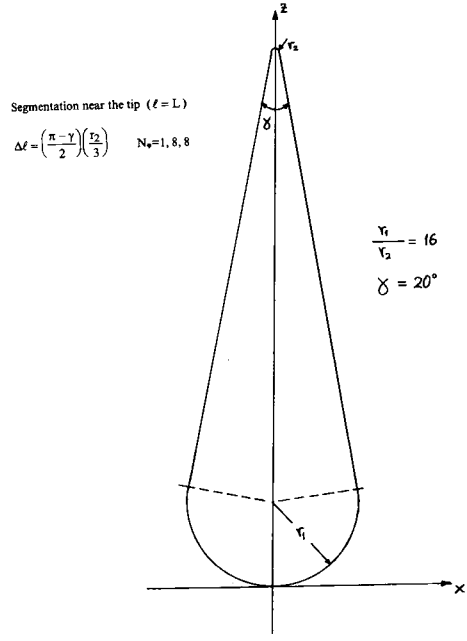

Figure 19. The sphere-cone-sphere scatterer.

2.6 and 2.26 and then falling abruptly to about 1.66 and 1.57, respectively, right at $\ell = L$ or $t = 0$. Here $t = (L - \ell)/\lambda$, same as in Figure 4.15 of [13]. Therefore, with about 546 patches we get an accurate representation for $|J_t|$, $|J_\varphi|$. This is the reason that only $N = 546$ was used in the case of tip-end incidence, Figure 21. For $\varphi = 0°$, $J_\varphi = 0$ and $J_t = J$; for $\varphi = 90°$ both $|J_\varphi|$ and $|J_t|$ are plotted. Our results in this case $(k\alpha = kr_1 = 1.26)$ are in excellent agreement with those of [13] obtained via the MFIE method.

We then treated a much larger shape, $kr_1 = 6.28$ $(r_1/\lambda = 1)$, $r_1/r_2 = 16$ and included angle $20°$. The results are shown in Figures 22, 23. The total number of patches was $N = 546$ and $N = 1194$ with an average $\lambda/(\Delta S)^{1/2} = 4.68$ and 6.93, respectively. Observations similar to those in the preceding case can be made. Away from the tip $|J_\varphi|$ and $|J_t|$ are accurately evaluated even with $N = 546$ patches. In this case, $kr_1 = 6.28$, and for tip-end incidence (Figure 23) the standing-wave behavior for $|J_t|$ is again observed in the base (or sphere-end) part of the surface.

4. CONCLUSIONS

By taking into account analytically the all important self-patch contribution to the surface integrals we have developed a reliable and computer-time-saving method of solving Maue's equation for axisymmetric perfectly conducting scatterers, well into the resonance region; this last claim may have to be restricted by excluding shapes with extreme changes in the radius of curvature. A few comments related to the characterization of "all important" for the self-patch contribution may be in order at this point. As mentioned in the Introduction, the integrands of the improper surface integrals appearing in Maue's equation exhibit a singularity not worse than $f(\vec{r}, \vec{r}')/R$ were $f(\vec{r}, \vec{r}')$ is a regular function of $\vec{r}, \vec{r}'$ [1–4, 7]. The singularity is integrable and this is sometimes termed as a weakly singular kernel. Consider now a subsurface of eight adjacent patches ΔS surrounding a central patch ΔS_0 and let us evaluate the contribution of these nine patches at the center $\vec{r} = \vec{r}_c$ of ΔS_0. By taking the total area of the nine patches small enough we can approximate $f(\vec{r}_c, \vec{r}')$ by $f(\vec{r}_c, \vec{r}_c) = \text{constant}$, for all $\vec{r}'$ in these patches; there remains the singular surface integral $\iint\limits_{\Delta S} \frac{1}{|\vec{r}' - \vec{r}_c|} = \iint\limits_{\Delta S} \frac{dS'}{R}$ and with $R > 0$ it is obvious that the self-patch

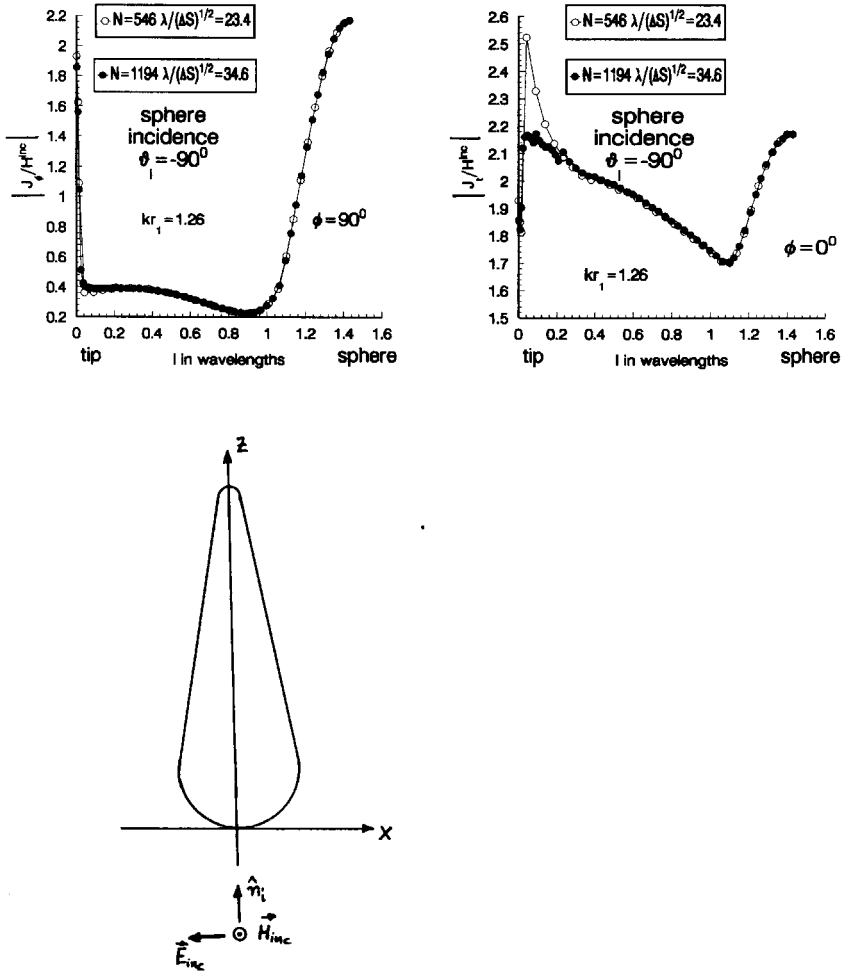

Figure 20. Normalized amplitudes of surface current density components $|J_\varphi/H^{\mathrm{inc}}|$ and $|J_t/H^{\mathrm{inc}}|$ vs $(L-\ell)/\lambda$ for a sphere-cone-sphere with $kr_1 = 1.26$, $r_1/r_2 = 16$ and 20° included angle and for sphere-end incidence. The plots for $N = 546$ and 1194 are superimposed.

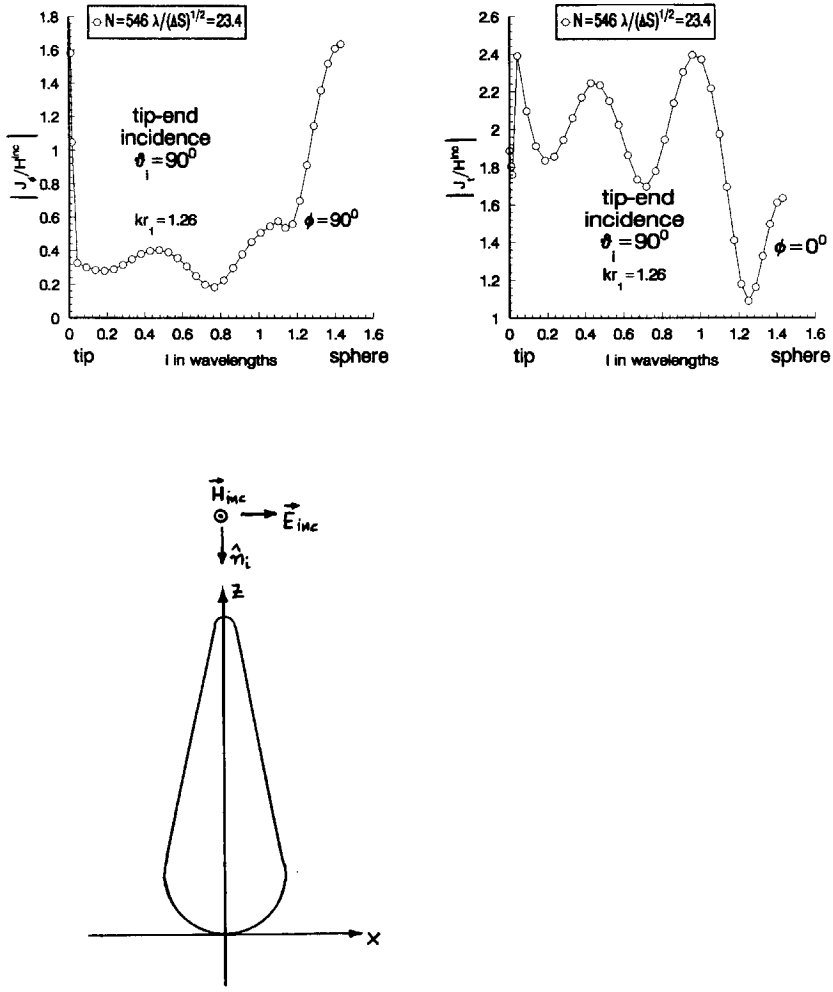

Figure 21. Same as Figure 20 but for tip-end incidence and for $N = 546$ patches.

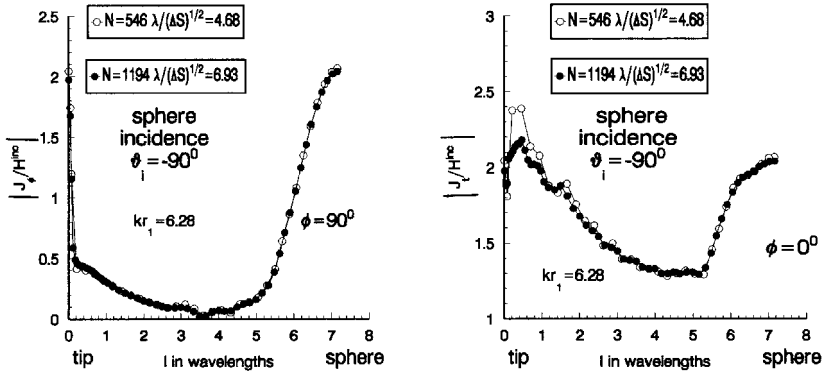

Figure 22. Same as Figure 20 but for a larger scatterer, $kr_1 = 6.28$.

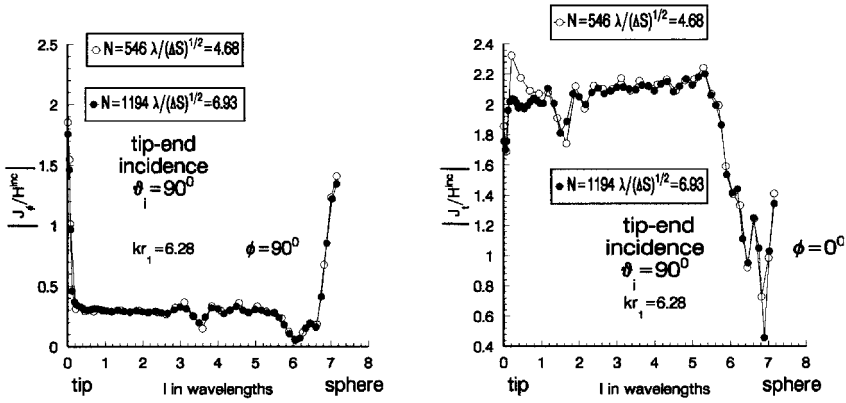

Figure 23. Same as Figure 21 but for a larger scatterer, $kr_1 = 6.28$.

contribution, for which R goes to 0 in the course of integration, predominates.

Other approaches based on "principal value" calculations, in effect ignore the self-patch contribution on the grounds that it vanishes in the limit $\Delta S_0 \to 0$. Although correct, this implies very small ΔS_0, therefore large number of patches N for S, and omission of the predominant contribution at least locally.

Another worthwhile observation that the numerical results revealed was the fact, already mentioned in connection with the spherical shape, that mode **A** was at least as efficient as mode **B** even when the contribution of the immediate neighboring patch was calculated. This was not obvious to us on the basis of the following "geometrical" argument: Consider two adjacent "square" patches ΔS_0, ΔS_1, of side α each; in the course of evaluating the contribution of ΔS_1 at the center $\vec{r}_c$ of ΔS_0 using mode **B**, R varies between $\alpha/2$ and $\alpha\sqrt{10}/2$; one would expect, therefore, mode **B** to provide a more accurate result than mode **A**, for which all values of R in ΔS_1 are substituted by α, the distance between the centers of the patches. A possible explanation for this rather unexpected result was proposed by Professor T. T. Wu of Harvard University: evaluations based on mode **B**, being approximate, violate the principle of reciprocity, something easily verified by alternating the patch of evaluation between ΔS_0 and ΔS_1; in contrast, results based on mode **A** obviously continue to satisfy reciprocity, since R_c is the same for either patch of evaluation. A further suggestion by Professor Wu, that restores reciprocity even with mode **B** evaluations, is to calculate average values of the surface integrals over ΔS_0 rather than mere values at its center; this requires an additional surface integral, but, it seems to be rather easy to carry it out, taking into account that the mode **B** formulas (23)–(25) provide values of the surface integrals at any point of ΔS, not merely at its center. However, such considerations, as well as others related to remarks made after equation (27) and connected with patches around the cyclical bottom $(\ell = 0)$ and top $(\ell = L)$ ones (for which $\varphi - \varphi'$ cannot, in general, be considered small to avoid very thin or elongated patches), are properly the subject of a subsequent paper.

ACKNOWLEDGMENT

The authors wish to acknowledge the very valuable comments of Professor T. T. Wu of Harvard University and to thank him for his suggestions of worthy steps that this investigation should take in the future. This work was supported in part by NATO CRG Programme SA.5-2-05 (CRG.951313) New.

REFERENCES

1. Maue, A. W., *Z. Physik 126,* 601–618, 1949.
2. Hönl, H., A. W. Maue, and K. Westpfahl, *Handbuch der Physik,* Vol. 25/1, 218–573, Springer-Verlag, Berlin 1961.
3. Van Bladel, J., *Electromagnetic Fields,* McGraw-Hill Book Co., Inc., New York, 1964.
4. Van Bladel, J., *Singular Electromagnetic Fields and Sources,* Clarendon Press, Oxford, 1991.
5. Yaghjian, A. D., "Augmented electric- and magnetic-field integral equations," *Radio Science,* Vol. 16, No. 6, 987–1001, Nov.-Dec. 1981.
6. Hsiao, G. C., and R. E. Kleinnman, "Mathematical foundations for error estimation in numerical solutions of integral equations in electromagnetics," *IEEE Trans. Ant. and Prop.,* Vol. AP-45, No. 3, 316–328, March 1997.
7. Kellog, O. D., *Foundations of Potential Theory,* Dover Publ., Inc., New York, 1953.
8. Marx, E., "Self-patch integrals in transient electromagnetic scattering," *IEEE Trans. Ant. and Prop.,* Vol. AP-33, No. 7, 763–767, July 1985.
9. Marx, E., "Neighboring-patch integrals in transient electromagnetic scattering," *IEEE Trans. Ant. and Prop.,* Vol. AP-33, No. 7, 768–773, July 1985.
10. King, R. W. P., R. E. Mack, and S. S. Sandler, *Arrays of Cylindrical Dipoles,* Cambridge University Press, 1968.
11. Kerker, M., *The Scattering of Light,* Academic Press, New York, 1969.
12. Ruck, G. T., D. E. Barrick, W. D. Stuart, and C. K. Krichbaum, *Radar Cross Section Handbook,* Plenum Press, New York, 1970.
13. Poggio, A. J., and E. K. Miller, "Integral equation solutions of three dimensional scattering problems," Chapt. 4 of *Computer Techniques for Electromagnetics,* edited by R. Mittra, Pergamon Press, Oxford, 1973.

14. Mautz, J. R., and R. F. Harrington, "Generalised network parameters for bodies of revolution," Syracuse University, Electrical Engineering Department, Contract No. F-19628-67-C-0233, Scientific Report No. 1, 1968.
15. Mautz, J. R., and R. F. Harrington, "H-field , E-field, and combined-field, solutions for conducting bodies of revolution," *AEU,* Vol. 32, 157–164, 1978.
16. Fikioris, J. G., "The EM field of constant current density distributions in parallelepiped regions," *IEEE Trans. Ant. and Prop.,* Vol. 46, No. 9, 1358–1364, September 1998.
17. Magoulas, A. N., *Scattering from Axisymmetric Perfect Conductors. A Hybrid Method of Solving Maue's Equation,* Ph. D. Thesis, Department of Electrical and Computer Engineering, National Technical University of Athens, Greece, 1999.